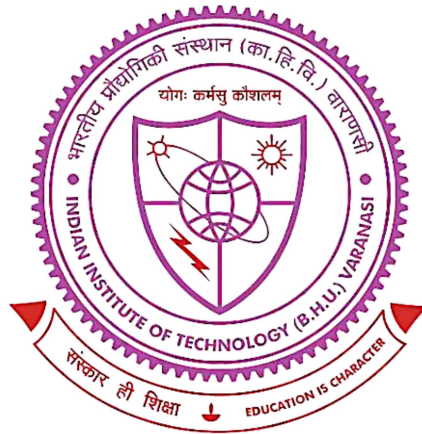


**3D self-assembled chessboard-like microstructural evolution in  
CoFeMn and CoFeGaMnZn oxide spinels and NdLiTiO<sub>3</sub>  
perovskites for nano-electronics/energy devices**



**Thesis submitted in partial fulfilment for the  
Award of Degree**

*Doctor of Philosophy*

**By**

*Avnish Singh Pal*

**DEPARTMENT OF METALLURGICAL ENGINEERING  
INDIAN INSTITUTE OF TECHNOLOGY  
(BANARAS HINDU UNIVERSITY)  
VARANASI – 221005  
INDIA**

**Roll No. 15141503**


**2022**



# CERTIFICATE

It is certified that the work contained in the thesis titled “**3D self-assembled chessboard-like microstructural evolution in CoFeMn and CoFeGaMnZn oxide spinels and NdLiTiO<sub>3</sub> perovskites for nano-electronics/energy devices**” by "Avnish Singh Pal" has been carried out under my supervision and that this work has not been submitted elsewhere for a degree.

It is further certified that the student has fulfilled all the requirements of Comprehensive, Candidacy and SOTA for the award of Ph.D. degree.



**Dr. Joysurya Basu**  
(Supervisor)  
Associate Professor  
Department of Metallurgical Engineering  
Indian Institute of Technology  
(Banaras Hindu University)  
Varanasi



## **DECLARATION BY THE CANDIDATE**

I, **Avnish Singh Pal**, certify that the work embodied in this Ph.D. thesis is my own bonafide work carried out under the supervision of **Dr. Joysurya Basu** for a period from **Dec 2015** to **July 2022** at the “**Department of Metallurgical Engineering**”, Indian Institute of Technology (BHU), Varanasi, India. The matter embodied in this Ph.D. thesis has not been submitted for the award of any other degree/diploma. I declare that I have faithfully acknowledged and given credits to the research workers wherever their works have been cited in my work in this thesis. I further declare that I have not willfully copied any other's work, paragraphs, text, data, results, etc., reported in journals, books, magazines, reports dissertations, thesis, etc., or available at websites and have not included them in this thesis and have not cited as my own work.



**Date :** July 20, 2022

**Place :** Varanasi

**(AVNISH SINGH PAL)**



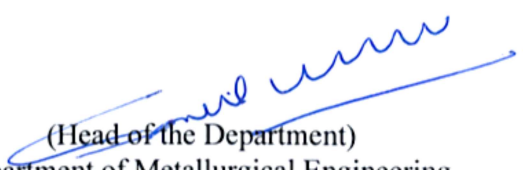
## **CERTIFICATE BY THE SUPERVISOR**

This is to certify that the above statement made by the candidate is correct to the best of my knowledge.



**Dr. Joysurya Basu**  
(Supervisor)  
Department of Metallurgical Engineering  
Indian Institute of Technology (Banaras Hindu University)  
Varanasi

**Forwarded by:**



(Head of the Department)  
Department of Metallurgical Engineering  
Indian Institute of Technology  
(Banaras Hindu University)  
Varanasi – 221005, India



## COPYRIGHT TRANSFER CERTIFICATE

---

**Title of the Thesis:** 3D self-assembled chessboard-like microstructural evolution in CoFeMn and CoFeGaMnZn oxide spinels and NdLiTiO<sub>3</sub> perovskites for nano-electronics/energy devices.

**Candidate's Name :** Avnish Singh Pal

## COPYRIGHT TRANSFER

---

The undersigned hereby assigns to the Indian Institute of Technology (Banaras Hindu University), Varanasi all rights under copyright that may exist in and for the above thesis submitted for the award of the *Doctor of Philosophy*.

**Date:** July 20, 2022

**Place:** Varanasi



(Avnish Singh Pal)

---

**Note:** However, the author may reproduce or authorize others to reproduce materials extracted verbatim from the thesis or derivative of the thesis for author's personal use provided that the source and the Institute's copyright notice are indicated.

## Acknowledgement

I want to inaugurate my acknowledgement statement by offering my gratitude to the almighty God for the wisdom he has showered over me that has made my path easy to this attainment.

I am expressing my sincere gratitude to my supervisor Dr Joysurya Basu, for imparting his knowledge and expertise in this work. I am very fortunate to have learnt the basics of materials characterization techniques and crystallography from him. He has not only trained me on transmission electron microscopy but also introduced me with related advanced characterization techniques, such as in-situ TEM, EELS, HAADF-STEM-XEDS, etc. In combination with hands on experience, he has also made me familiar with essential analytical tools such as multislice image simulation (JEMS), crystal structure identification (Rietveld refinement) and other analytical software. His emphasis over squeezing the gathered data at the fullest, has implanted a sense of critical thinking and developed the ability of thinking out of the box. He has always advised me to prefer quality over quantity, which immensely benefited me in publishing my research work in reputed journals. In simple words, his amiable and enthusiastic nature and clear vision has helped me greatly in uplifting my understanding of such an intricate subject. I am extremely thankful to him for his untiring support throughout my Ph.D. journey, specially the push he gave me every time I have got stuck. It is my pleasure working under his guidance.

It is my privilege to express my heartfelt gratitude to him for giving me the latitude to perform various experiments irrespective of their success probability, which has immensely helped me in developing concept out of the book. His innovative approach towards research, always enhances my propensity toward research and inspired me to remain positive and be patient in all ups and downs. He is a thorough observer and a patient researcher, he listens to my all queries and tries to turn them into a logical discussions that always boosts up my confidence. His approach of putting the intricate things in simple and elusive manner has always inspired me to attain perfection in my work. I am indebted to him for inspiring guidance, persistent encouragement throughout the course of this work.

I would also like to convey my thanks to Prof. S. Lele, Prof. G.V.S. Sastry, Prof. N. K. Mukhopadhyay, Prof. Vakil Singh and Prof. R K Mandal for fruitful discussions and, former Heads of the Department for their kind support. I thank Prof. Sunil Mohan, the current Head of the Department for his valuable contribution.

I also want to show respect to the all faculty members of Department of Metallurgical Engineering, IIT (BHU) for creating such a wonderful environment for research. I would also like to express my gratitude to the entire non-teaching staff of the Metallurgical Engineering Department of IIT BHU.

I sincerely thank Dr K.G. Pradeep, Department of Metallurgical and Materials Engineering, IIT Madras, for extending me support for correlative microscopy and FIB sample preparation. It is my pleasure to thank Prof. Kevin M. Knowles, Department of Materials Science and Metallurgy, University of Cambridge, for involving in frequent and long discussion sessions, which has helped me improving my knowledge of crystallography to take my work up to next level. My heartedly thanks to Dr. Surendra Kr. Makineni, IISc, Bangalore, for providing me sophisticated instrumental facilities. I gratefully acknowledge Dr. Imteyaz Ahmed, Ceramic Engineering, IIT BHU, for letting me avail the high temperature furnaces for long heat treatment hours. I am extremely thankful to Prof. N. Ravishankar, IISc, Bangalore, for letting me avail the aberration corrected TEM (Titan 300) facility. Working with all of them have been a great learning experience.

I am grateful to my present and former labmates, Dr. Manish Singh, Dr. Vikas Shivam, Dr. Raj Bahadur, Dr. Vivek Pandey, Dr. Yagnesh, Dr. Raj, Dr. Asnit, Ankit, Shubham, Roopchand, Saarika, Soham, Saptarshi, Satyam, Sandeep, Urvashi, Deepak, Sujeet, Ankur, and Pavithra, for their cheerful company. I also want to convey my thanks to Lalit Kr. Singh and Aman for their unconditional support and readiness for any kind of help.

At personal front, I wish to express my sincere gratitude and indebtedness to my family for their blessings, care, encouragement and moral support throughout this journey.

I would also like to thank EMSI, Research & Development (IIT BHU), Mrs. Indira Anathachari endowment fund, and IIM Trust for extending me financial assistance for attending the national and international Conferences.



**(Avnish Singh Pal)**



## TABLE OF CONTENTS

---

### Table of contents

Abbreviations.....	xiii
Symbols.....	xiv
Preface.....	xv
1. Chapter 1.....	1
1.1 Self-assembly.....	4
1.1.1 Classification of self-assembled structures.....	4
1.1.1.1 Static/Equilibrium self-assembly (SSA).....	5
1.1.1.2 Dynamic/non-equilibrium self-assembly (DySA).....	5
1.1.2 Applications of SA in nanoarchitectonics.....	7
1.2 Metamaterials (MM).....	8
1.3 Self-assembled materials Vs Metamaterials.....	10
1.4 Theory of phase separation.....	11
1.4.1 Chemical phase separation.....	11
1.4.1.1 Spinodal decomposition.....	12
1.4.1.2 Nucleation and growth.....	14
1.4.1.3 Pseudospinodal decomposition.....	14
1.4.2 Order-disorder transformation.....	15
1.4.2.1 Charge ordering (CO).....	17
1.4.2.2 Magnetic ordering (MO).....	17
1.4.3 Structural phase separation.....	18
1.4.4 Electronic phase separation.....	19
1.5 History of self-assembled CB microstructures.....	20
1.5.1 Proposed theory for self-assembled 3D chessboard microstructures.....	20
1.5.1.1 Tweed-like structure to CB-like microstructure.....	21
1.5.1.2 J-T distortion assisted CB-like microstructural evolution.....	23
1.5.1.3 Order-disorder assisted CB-like microstructure.....	24
1.5.1.4 Octahedra tilting assisted CB-like microstructure.....	26
1.5.1.5 CB-like arrangements by pseudouniform ordering in superspace.....	27
1.6 Applications of CB-like microstructure.....	31
1.6.1 High density memory applications.....	31
1.6.2 Thermoelectric applications.....	33
1.6.3 Applications of self-assembled 3D CB microstructure in ASSLBs.....	33
References.....	36
2. Chapter 2.....	47
2.1 Material selection.....	48
2.2 Material synthesis.....	48
2.2.1 Synthesis of CB-like microstructure in spinel manganites.....	49

## TABLE OF CONTENTS

---

2.2.2	Synthesis of CB-like microstructure in $\text{Li}_{3x}\text{Nd}_{(2/3-x)}\square_{(1/3)-2x}\text{TiO}_3$ .....	50
2.3	Characterization techniques.....	50
2.3.1	XRD analysis.....	51
2.3.2	TEM analysis.....	51
2.3.3	APT analysis.....	52
2.4	Sample Preparation.....	54
2.4.1	XRD sample preparation.....	54
2.4.2	TEM sample preparation.....	54
2.4.3	APT sample preparation.....	54
2.5	Physical properties characterization.....	55
	References.....	57
3.	Chapter 3.....	59
3.1	Introduction.....	60
3.2	Materials and methods.....	61
3.3	Results and discussion.....	62
3.3.1	X-ray diffraction analysis.....	62
3.3.2	Diffraction contrast and Z-contrast imaging.....	64
3.3.3	Phase contrast imaging.....	75
3.4	Conclusions.....	78
	References.....	80
4.	Chapter 4.....	83
4.1	Introduction.....	84
4.2	Materials and methods.....	85
4.3	Results and discussion.....	86
4.3.1	X-ray diffraction analysis.....	86
4.3.2	Diffraction contrast imaging and Z-contrast imaging.....	88
4.3.3	Orientation relationship establishment.....	90
4.3.4	Observation of subdomains, their orientation relationship and chemistry.....	95
4.3.5	Clarification of CB-like appearance in 3D.....	97
4.3.6	Reconstruction of 3D microstructure via correlative microscopy.....	98
4.4	Conclusions.....	104
	References.....	105
5.	Chapter 5.....	109
5.1	Introduction.....	110
5.2	Materials and methods.....	113
5.3	Result and discussion.....	115
5.3.1	Microstructural characterization.....	115
5.3.1.1	XRD analysis.....	115
5.3.1.2	TEM analysis.....	119
5.3.1.3	3D re-construction of microstructure by APT.....	122

## TABLE OF CONTENTS

---

5.3.2	Effect of CB-like microstructural evolution on Electrochemical properties.....	124
5.4	Conclusions.....	127
	References.....	129
6.	Chapter 6.....	131
6.1	Introduction.....	132
6.2	Materials and methods.....	135
6.3	Results and discussion.....	136
6.3.1	XRD analysis.....	136
6.3.2	Diffraction contrast microscopy.....	138
6.4	Conclusions.....	145
	References.....	147
7.	Chapter 7.....	149
7.1	Conclusions.....	150
7.2	Scope and suggestion for future work.....	153
8.	List of publications.....	155
9.	List of conference presentations.....	156

---

## List of Figures

- Figure 1.1 A variety of patterned nanostructures obtained by (a, b) array of triangular metal dots 3  
obtained after removal of a single layer nanosphere mask and double layer nanosphere  
mask by multiple-patterning nanosphere lithography followed by oxygen plasma  
etching, respectively (c) SEM micrograph showing the self-assembly of nanospheres  
inside the templates to form multiple layers (d) self-assembly of water molecules in  
the form of snowflake (e, f) TEM images of the as synthesized polyhedron-shaped and  
cuboid-shaped  $\text{MnFe}_2\text{O}_4$  nanoparticles synthesized through shape-induced texturing of  
the particles through self-assembly, respectively (g) CNT growth on  $\text{SiO}_2/\text{Si}$  substrates  
via ethanol CVD, here  $\text{W}_6\text{Co}_7$  alloy nanoparticles help in controlling chirality by lipid  
supramolecular self-assembly process (h) fabrication of 3D building blocks in desired  
shapes using the DNA-directed self-assembly (i) TEM image of the CdSe/CdS  
quantum dots (QD) suspended in octane (left), patterned placement of QD through e-  
beam patterning (right) (j) Schematic of DNA origami nanostructures formed via the  
lipid-bilayer-assisted self-assembly technique, AFM image of the lattice.
- Figure 1.2 Equilibrium/static (SSA) and non-equilibrium/dynamic (DySA) self-assemblies in a 6  
binary system. SSA, arranged basic building blocks in a “static” structure without any  
energy exchange through it. The arrangement does not change due to any  
thermodynamic variation. In DySA, a flux of energy in any form (here  $dE_1$ ) flows  
through the system that maintains the structure in any of its metastable states. These  
metastable states depend on the magnitude of flux, any manipulation in the energy/flux  
( $dE_1-dE_2$ ) may alter the arrangement to other suitable metastable state.
- Figure 1.3 (a) Designing Carbon-based bioelectronics devices such as tissue stimulator by 7  
utilizing self-assembly for Parkinson’s or cardiac problems. (b) schematic  
representation of anode (grey), cathode (blue) and separator (green) with  
corresponding molecular structure of each layer in a 3D battery.
- Figure 1.4 (a) A metamaterial possessing negative index is fabricated by SRRs and wires 9  
deposited lithographically on the opposite sides of a standard circuit board. (b) a graph  
obtained by Snell’s law experiment shows power detected as a function of angle  
performed on a negative index sample and a Teflon sample.
- Figure 1.5 Various type MM devices developed for a range of frequency from radio to near optical 10  
frequencies. Frequency ranges are mentioned in left column, middle column shows  
photo of corresponding MM, and third column summarizes their performance details.
- Figure 1.6 Schematic representation of spinodal decomposition (a) spinodal and binodal curves 13  
(b) Gibbs free energy Vs. Composition graph showing point of inflection and  
equilibrium composition at  $X_1$  and  $X_2$ .

## LIST OF FIGURES

Figure 1.7	Schematic representation of two APB in Au-Cu alloy (a) corresponding electron diffraction pattern along [001] zone axis showing satellite spots.	16
Figure 1.8	The exchange interaction for the Mn spins in layered double perovskite Ba <sub>2</sub> MnTeO <sub>6</sub> (a) J <sub>1</sub> represents an in-plane exchange interaction with nearest neighbor. Whereas J <sub>2</sub> and J <sub>3</sub> are out-of-plane interactions with nearest and next-nearest neighbor.(b) in such compounds these interaction may produce four types of magnetic interactions, e.g., FM (ferromagnetic), AFM1 (anti ferromagnetic), AFM2, and AFM3.	18
Figure 1.9	SEM images of K <sub>0.8</sub> Fe <sub>1.6+x</sub> Se <sub>2</sub> superconducting sample showing presence of two phases as stripe-like patterns having interfaces along [110] and [1 $\bar{1}$ 0] directions. (b) phase contrast HR TEM image illustrating phase separated domains at nanoscale. (c) Alternative appearance of the K <sub>0.8</sub> Fe <sub>1.6</sub> Se <sub>2</sub> and K <sub>y</sub> Fe <sub>2</sub> Se <sub>2</sub> phases.	19
Figure 1.10	(a) Bright field diffraction contrast image of precursor tweed that work as template for resultant chessboard structures shown in (b) along [100] (c) a 3D schematic chessboard nanowires, in which dark domains are representing tetragonal domains with two orientations (marked by arrow). In the (c) white domains are depicting cubic phase. (d) graph representing the variation of free-energy-versus-composition in A and B composition range for the tetragonal and cubic phases.	22
Figure 1.11	Diffraction contrast images of Co <sub>0.6</sub> Fe <sub>0.9</sub> Mn <sub>1.5</sub> O <sub>4</sub> sample, sintered at 1473 K for 20 hours followed by quenching and annealing at 648 K for (a) 0 hours, (b) 80 hours, (c) 340 hours and (d) 730 hours. Corresponding electron diffraction patterns are shown in the insets of (a), and (d). (e) Schematic representation of J-T distortion when Mn <sup>+3</sup> is octahedrally coordinated with oxygen atoms causing splitting of d <sup>4</sup> in to degenerate subshells.	24
Figure 1.12	DF image of typical L <sub>10</sub> +L <sub>12</sub> microstructure oriented near [001], by selecting 110 spot, depicting the patchwork of I, II and III type areas. In area type I, only L <sub>12</sub> domains are illuminated while, L <sub>10</sub> domains are out of contrast. Similarly, other two orientation variant of L <sub>10</sub> +L <sub>12</sub> patchworks (type II and type III) are denoted by arrows. (b) phase diagram of Co-Pt system in range 50-75 at.% pt. (c) schematic of L <sub>12</sub> and L <sub>10</sub> ordered structures, black and white atoms are representing A and B atoms.	25
Figure 1.13	(a) Phase contrast high resolution image of Li <sub>0.15</sub> Nd <sub>0.61</sub> TiO <sub>3</sub> sample sintered at 1250 °C followed by annealing (20 °C/hour) along [001] zone axis and corresponding fourier transformation (inset) (b) crystal structure of LiNdTiO <sub>3</sub> showing ordering in [001] direction. (c) schematic depicting alternative modulation of strain manifestation of tilt twinning of BO <sub>6</sub> octahedra.	27
Figure 1.14	(a) Expansion of fraction between 1/3 and 1/2 up to fifth level by Farey tree method (b) Schematic representation of Farey tree model showing 1D arrangement of minority motifs considering GLG repulsive model (c) Stripe pseudouniform ordering for x = 5/12 made after lattice stripe decomposition in a combination of two basic tiles of x = 1/2 and 1/3 (left), corresponding Farey tree sequencing 5/12: 1/2 ⊕ 1/2 ⊕ 1/3 ⊕ 1/2	29

## LIST OF FIGURES

---

	<p><math>\oplus</math> 1/3 (left), describing a supercell (right) (d) 2D tiling of <math>x = 1:1, 1:3, 1:6</math> ratio of solute and minority motifs (e) Although, for uniform distribution <math>A_{1-x}B_x</math> where <math>x=1/8</math> two alternative orderings are possible considering a uniform square lattice. However lattice gas model prefers former one. (f) conventional description of superspace of 1D ordering showing concatenation of monatomic columns. (g) Fourier spectra of pseudouniform stripe corresponding to <math>x = 5/12</math>.</p>	
Figure 1.15	Checkerboard-like pseudouniform orderings for $x = 5/12$ (a) obtained after energy optimization for larger range of the repulsive potential (b) their representation as pseudouniform arrangements of A motifs $x=1/2$ within a halved lattice (bcc) with a relative density of $y = (1 - 2x)$ .	30
Figure 1.16	(a) Cross-sectional SEM image of a state-of-the-art PMR media with a data storage density $\sim 800$ Gb/inch <sup>2</sup> , here 1 bit is marked by white dotted lines (b) A schematic layover on an actual SEM image of a realistic media grains representing recorded transitions, where black corresponds to $M = 1$ , white corresponds to $M = -1$ , and grey is $M = 0$ .	32
Figure 2.1	Heat treatment program for all the manganite spinel systems.	49
Figure 2.2	Heat treatment to develop CB-like microstructure in $\text{Li}_{3x}\text{Nd}_{(2/3)-x}\square_{(1/3)-2x}\text{TiO}_3$ perovskite system.	50
Figure 2.3	Rotation calibration of Tecnai G <sup>2</sup> T20 TEM with the help of ZnO nanowire, Figure shows superimposition of diffraction pattern and the corresponding bright field image along $[01\bar{1}0]$ zone axis. Schematic representation of e-beam travelling from filament to sample in a transmission microscope.	52
Figure 2.4	Working line diagram of a Local Electrode Atom Probe.	53
Figure 2.5	TEM sample preparation by drop cast method.	54
Figure 2.6	Sample preparation steps for APT analysis (a-d) SEM image showing groove formation and lifting the area of interest (e-j) SEM image showing shaping of lifted sample by laser sharpening to obtain needle with a sharp apex.	55
Figure 2.7	Stepwise representation of sample preparation for electrochemical analysis of $\text{LiNdTiO}_3$ samples.	56
Figure 3.1	Multiple display of powder XRD patterns of $\text{ZnGaMnO}_4$ , $\text{Co}_{0.6}\text{Fe}_{0.8}\text{Mn}_{1.6}\text{O}_{4+\delta}$ ( $\delta \ll 1$ ) and $\text{Co}_{0.6}\text{Fe}_{0.8}\text{GaMn}_{2.6}\text{ZnO}_{8+\delta}$ ( $\delta \ll 1$ ) after sintering at 1250 °C for 24 hours followed by ageing at 375 °C for 150 hours. The XRD patterns indicate the presence of the cubic $\text{Fd}\bar{3}\text{m}$ $\text{ZnGa}_2\text{O}_4$ and tetragonal $\text{I4}_1/\text{amd}$ $\text{ZnMn}_2\text{O}_4$ phases in the pattern of $\text{ZnGaMnO}_4$ , and the presence of the cubic $\text{Fd}\bar{3}\text{m}$ $\text{CoFe}_2\text{O}_4$ and tetragonal $\text{I4}_1/\text{amd}$ $\text{CoMn}_2\text{O}_4$ phases in the $\text{Co}_{0.6}\text{Fe}_{0.8}\text{Mn}_{1.6}\text{O}_{4+\delta}$ pattern. The cubic spinel peaks are marked with black dotted lines with reference to cubic $\text{CoFe}_2\text{O}_4$ and the tetragonal spinel peaks are marked with red dotted lines with reference to tetragonal $\text{CoMn}_2\text{O}_4$ . These two patterns have been indexed with respect to the conventional unit cell descriptions for the two tetragonal phases. The XRD pattern of $\text{Co}_{0.6}\text{Fe}_{0.8}\text{GaMn}_{1.6}\text{ZnO}_{8+\delta}$ also shows signs of separation	63

## LIST OF FIGURES

---

- of similar cubic and tetragonal phases. Shifting in the  $(103)_t$  and  $(224)_t$  peaks of the tetragonal phase in the XRD pattern of  $\text{Co}_{0.6}\text{Fe}_{0.8}\text{GaMn}_{1.6}\text{ZnO}_{8+\delta}$  with respect to  $\text{ZnMn}_2\text{O}_4$  and  $\text{CoMn}_2\text{O}_4$  is indicative of slight changes in the  $a$  and  $c$  lattice parameter.
- Figure 3.2 (a) TEM diffraction contrast bright field image from the centre of the  $\text{Co}_{0.6}\text{Fe}_{0.8}\text{Mn}_{1.6}\text{O}_{4+\delta}$  pellet sintered at 1250 °C for 24 hours followed by ageing at 375 °C for 150 hours showing two sets of co-existing tetragonal domains. Domain boundaries are parallel to  $(0\bar{2}2)$  interface planes of the FCT unit cell. (b) Electron diffraction pattern from (a) showing twinning on the common  $(0\bar{2}2)$  planes of the two domains. (c) HAADF-STEM-XEDS Z-contrast compositional mapping showing the segregation of Fe and Mn to alternating twinned regions. (d) Bright field image from the periphery of the  $\text{Co}_{0.6}\text{Fe}_{0.8}\text{Mn}_{1.6}\text{O}_{4+\delta}$  pellet after sintering and ageing as described for (a) showing cuboidal nanodomains observed slightly off axis from a  $[100]$  zone. (e) Electron diffraction pattern from the region in (d) consistent with the presence of cubic and tetragonal phases. The interfaces of the squared nanodomains are along  $\{022\}$  family of planes with respect to the FCC and FCT unit cells of the cubic and tetragonal phase. (f) HAADF-STEM-XEDS Z-contrast compositional map from the cuboidal nanodomains showing the onset of separation of Fe and Mn in two neighboring nanodomains. 65
- Figure 3.3 (a) Diffraction contrast image of the  $\text{Co}_{0.6}\text{Fe}_{0.8}\text{Mn}_{1.6}\text{O}_{4+\delta}$  ( $\delta \ll 1$ ) after heat treatment at 1250 °C for 24 hours followed by quenching in ice water. Subsequently it was aged at 375 °C for 150 hours. In the diffraction contrast image alternate bands of Fe-rich and Mn-rich domains are observed. The width of the individual bands is  $\sim 70$  nm. STEM-HAADF-EDS mapping is shown for (b) Fe, (c) Mn, (e) O and (f) Co. Co and O are uniformly distributed while Fe and Mn are alternately distributed in the bands. (d) Nano-beam electron diffraction pattern from the white point in the dark band in (a). In the diffraction pattern the tetragonal symmetry of the band is clearly observed. 67
- Figure 3.4 (a) TEM bright field image from the centre of the  $\text{ZnGaMnO}_4$  pellet after sintering at 1250 °C for 24 hours and subsequent ageing at 375 °C for 150 hours. A striped microstructure is apparent arising from the presence of two sets of domains. (b) Electron diffraction pattern from (a) indexed with respect to the doubly primitive FCT unit cell showing that twinning has occurred on  $(022)$  interface planes. (c) HAADF-STEM-XEDS Z-contrast compositional map showing the segregation of Ga and Mn to alternating twinned regions. (d) Bright field image from the periphery of the same pellet showing a chessboard-like morphology with  $(0\bar{2}2)$  and  $(\bar{2}0\bar{2})$  twin planes denoted by dotted lines. (e) Split in the  $\{202\}$  family of spots in the corresponding rotationally oriented diffraction pattern along the  $[1\bar{1}\bar{1}]$  zone axis showing the twinned orientation relationship between the domains. (f) HAADF-STEM-XEDS Z-contrast compositional mapping of Zn in the region shown in (c). It is evident that the Zn is almost uniformly distributed within the two twinned regions. 69

## LIST OF FIGURES

Figure 3.5	(a) HAADF image (b) diffraction contrast bright field image of the ZnGaMnO <sub>4</sub> after heat treatment at 1250 °C for 24 hours followed by quenching in ice water. Subsequently this was aged at 375 °C for 150 hours. In the HAADF and the bright field image an alternate banded structure is observed. STEM-HAADF-EDS maps are shown for (c) Ga+Mn overlay (d) Zn (e) Mn and (f) Ga. The alternate bands of Mn and Ga rich domains are ~70 nm wide.	70
Figure 3.6	(a) TEM bright field image from the centre of the Co <sub>0.6</sub> Fe <sub>0.8</sub> Mn <sub>1.6</sub> ZnGaO <sub>8+δ</sub> ( $\delta \ll 1$ ) pellet after sintering at 1250 °C for 24 hours and subsequent ageing at 375 °C for 150 hours. Twinned regions are evident. Each region is internally twinned on {202} <sub>FCT</sub> planes. (b) Electron diffraction pattern from (a) along a $[\bar{2}33]$ direction. (c) Bright field image from the periphery of the pellet showing a chessboard-like morphology, with alternating dark and bright nanodomains. (d) electron diffraction pattern from (c) indicating that within this chessboard-like morphology twinning has occurred on (202) <sub>FCT</sub> planes in (c).	71
Figure 3.7	STEM-HAADF-EDS mapping of the Co <sub>0.6</sub> Fe <sub>0.8</sub> GaMn <sub>2.6</sub> ZnO <sub>8+δ</sub> ( $\delta \ll 1$ ) after heat treatment at 1250 °C for 24 hours followed by quenching in ice water. Subsequently this was aged at 375 °C for 150 hours. In the HAADF image in (a) very faint linear contrast corresponding to the twins can be observed. EDS maps corresponding to (b) O (c) Mn (d) Fe (e) Co (f) Ga and (g) Zn show uniform distribution, indicating that the MCO after this aging treatment does not undergo significant composition separation.	73
Figure 3.8	XEDS spectrum of the Co <sub>0.6</sub> Fe <sub>0.8</sub> GaMn <sub>2.6</sub> ZnO <sub>8+δ</sub> ( $\delta \ll 1$ ) after heat treatment at 1250 °C for 24 hours followed by quenching in ice water. Subsequently this was aged at 375 °C for 150 hours. Compositions in wt% and in at% obtained after the background correction are given to the right of the spectrum. These are consistent with the starting composition, so that the relative ratios of different elements are also maintained.	75
Figure 3.9	(a) Phase contrast high-resolution image of Co <sub>0.6</sub> Fe <sub>0.8</sub> Mn <sub>1.6</sub> O <sub>4+δ</sub> ( $\delta \ll 1$ ) along $[\bar{1}12]$ zone axis after heat treated at 1250 °C for 24 hours followed by quenching in ice water and after a subsequent aging at 375 °C for 150 hours. In the same image, simulated HR image is overlaid on experimental image (surrounded by solid white rectangle), whereas subdomains are marked with dotted yellow rhombus, and their presence can be visualized by the variation in contrast in the image (the interfaces are marked with cyan arrows), (b) corresponding defocus-thickness map generated by Multislice simulation method performed with voltage = 200kV, C <sub>s</sub> = 1.2 mm and $\Delta f_{sch} = -65.83$ nm. parameters used. (c) perspective view of unit cell of CoFe <sub>2</sub> O <sub>4</sub> along $[\bar{1}12]$ .	76
Figure 3.10	(a) Phase contrast high-resolution image of Co <sub>0.6</sub> Fe <sub>0.8</sub> Mn <sub>1.6</sub> O <sub>4+δ</sub> ( $\delta \ll 1$ ) along $[\bar{1}12]$ zone axis after heat treatment at 1250 °C for 24 hours followed by quenching in ice water and a subsequent aging at 375 °C for 150 hours. In the same image, simulated HR image is overlaid on experimental image (surrounded by solid white rectangle), (b) corresponding defocus-thickness map generated by multislice simulation method	78

## LIST OF FIGURES

---

- performed with voltage = 200kV,  $C_s = 1.2$  mm and  $\Delta f_{sch} = -65.83$  nm. parameters used.
- (c) perspective view of unit cell of  $CoFe_2O_4$  along  $[\bar{1}11]$ .
- Figure 4.1 X-ray diffraction patterns of  $Co_{0.6}Fe_{0.8}Mn_{1.6}O_{4+\delta}$ , where  $\delta \ll 1$  after sintering at 1250 °C for 24 hours and subsequent quenching: (a) aged at 375 °C for 250 hours after quenching; (b) 0 hours/as-quenched. (c) Bright-field TEM image of sample aged for 250 hours and (d) the corresponding orientationally aligned diffraction pattern. (e) Bright-field TEM image of the same sample with (f) the corresponding orientationally aligned diffraction pattern showing the cross-over of the two sets of twins. 87
- Figure 4.2 Diffraction contrast images and corresponding diffraction patterns from the two twin variants that lead to the formation of a CB nanostructure in the  $Co_{0.6}Fe_{0.8}Mn_{1.6}O_{4+\delta}$  where  $\delta \ll 1$ , which was heat treated at 1250 °C for 24 hours, followed by quenching and ageing for 25 hours at 375 °C. The cross-over of two twin variants in (b) leads to the formation of the CB nanostructure. In the corresponding [100] electron diffraction pattern in (e) both the 022 type of spots are visible. Tilting  $\sim 3^\circ$  away from [100] makes twin variant I visible in (a) and in the corresponding diffraction pattern in (d) only 022 systematic spots are visible. Tilting  $\sim 3^\circ$  in the other direction away from [100] makes the twin variant II visible in (c) and in the corresponding diffraction pattern in (f) only  $0\bar{2}2$  systematic spots are visible. This confirms that the CB nanostructures initially forms by cross penetration of perpendicular twins and continuous rod like appearance is often the inability to see the other twin variant. 89
- Figure 4.3 (a) Bright-field TEM image and corresponding (b) rotationally aligned diffraction pattern from the  $Co_{0.6}Fe_{0.8}Mn_{1.6}O_{4+\delta}$ , where  $\delta \ll 1$  from the sintered, quenched and aged sample. (c) STEM-EDS composition map of the same sample showing separation of Mn and Fe within the neighbouring domains. (d-f): nanobeam electron diffraction pattern from (d) the cubic domain marked as C1, and (e) the tetragonal domain marked as T2 (f) vertical interface of C2 and T2 in (a). 91
- Figure 4.4 Bright field image of the CB nanostructure and nano-beam electron diffraction patterns from the nanodomains and the interfaces in  $Co_{0.6}Fe_{0.8}Mn_{1.6}O_{4+\delta}$  where  $\delta \ll 1$ . This sample was heat treated at 1250 °C for 24 hours, followed by quenching and ageing for 250 hours at 375 °C. Nanodomains are marked with 'A', 'B', 'C', 'D', 'E', 'F' and 'G' and their corresponding nano-beam diffraction patterns are given in (A-E, G). The nano-beam diffraction pattern from the interface of the domain 'A' and domain 'B' is given in 'AB' and the same from the domain 'F' and domain 'B' is given in 'FB'. Spot splitting is observed in the diffraction patterns from the interfaces indicating a relative rotation of  $5.2^\circ$  between the adjacent domains. Rotated cubic (C1, C2) and tetragonal (T1, T2) variants are observed from the diffraction patterns from the nanodomains and [004] of T1 is perpendicular to [004] of T2. 93
- Figure 4.5 (a) Composite [100] reciprocal lattice projection (up to first order reflections) of two cubic domains (C1 and C2) and two tetragonal domains (T1 and T2) leading to the splitting of reflections in the diffraction pattern from the CB nanostructure (b) 3D 94

## LIST OF FIGURES

---

- representation of the cubic and the tetragonal domains with in-plane and out-of-plane rotations, (c)-(e) systematic truncation of a cubic lattice that leads to the formation of octahedra with eight {220} surfaces (f) arrangement of octahedra in 3D that will appear to be a CB nanostructure from  $\langle 100 \rangle$  directions.
- Figure 4.6 (a) TEM dark field image of the CB domain taken from a  $\bar{4}20$  reflection, (b) the corresponding diffraction pattern along  $Z = [1\bar{2}\bar{2}]$ . Subdomains within the CB domains are visible. (c) STEM-EDS composition map from the CB domain showing composition separation between Fe and Mn. This is a tilted image of the CB nanostructure. (d) TEM image showing continuous rod like appearance, tilted to (e) where it is now showing a split domain contrast. (f) STEM-EDS composition map of the image in (e) where composition separation between Fe and Mn can be observed. 96
- Figure 4.7 (a) Corner and edge sharing network of irregular octahedra in which the domains in yellow and transparent blue color represent two phase separated domains. The 2D projection of the same network along (b) [001] (c) [010] and (d) [100]. 97
- Figure 4.8 Three-dimensional elemental distribution map of Fe, Co, Mn and O obtained using APT from an analyzed volume of  $64 \times 64 \times 1120 \text{ nm}^3$  and contour plot corresponding to Fe 24 at.% and Mn 29 at.% iso-concentration surface (top image). It shows a uniform distribution of Co and O with partitioning of Fe and Mn. 99
- Figure 4.9 (a), (b) Three-dimensional elemental map of Fe and Mn represented by their respective iso-concentration surfaces in two different orientations. (c) 1D composition depth profile of Fe, Mn, Co and O from the middle of the tip shown in the inset along the direction of the arrow. (d) Proximity histogram corresponding to Fe 24 at.% and Mn 29 at.% iso-concentration surface from the interface marked in square box. 100
- Figure 4.10 (a) Fe 24 at. % iso-concentration surface, (b) enlarged view of 10 nm cylindrical region of interest in (a) from the middle of the APT tip, (d) magnified version of single Fe-rich domain, (c) 1D composition depth profile of Fe, Mn, Co and O from (d). Intensity variation along (e) x-direction and (f) y-direction of the nanodomains within the plane of the page as observed within the green box in (d). 102
- Figure 4.11 (a) and (b) Two different ( $180^\circ$  rotated) orientations of Fe 24 at.% iso-concentration surface (c) Fe 24 at.% and Mn 29 at.% iso-concentration surface, (d) Fe 24 at.% iso-concentration surface showing the CB nanostructure at the middle, (e) Fe and Mn iso-concentration surface showing the CB nanostructure at the middle of the APT tip, (f) 10 nm cylindrical region (cyan color rod) of interest of Fe iso-concentration surface in (b), (g), (h): schematic representations of 2D and 3D nanostructured CB, respectively, (i) 1D composition profile of Fe, Mn, Co, O along the arrow in (f). 103
- Figure 5.1 XRD patterns of  $\text{Li}_{3x}\text{Nd}_{(2/3-x)}\square_{(1/3-2x)}\text{TiO}_3$  samples after sintering at  $1250^\circ\text{C}$  followed by annealing in air atmosphere (a) stack of XRD pattern for  $x = 0.05, 0.08, 0.12$  and  $0.16$ , sequentially from bottom to top (b) magnified view of Rietveld refined XRD 115

## LIST OF FIGURES

---

- pattern corresponding to  $x = 0.16$  in a  $2\theta$  range from  $45^\circ$  to  $52^\circ$  and (c) a magnified view of stacked patterns for all four values of  $x$  in a  $2\theta$  range from  $32^\circ$  to  $36^\circ$ .
- Figure 5.2 Rietveld refined XRD patterns of  $\text{Li}_{0.48}\text{Nd}_{0.5}\text{TiO}_3$  sample (a) after sintering at  $1250^\circ\text{C}$  117  
follow by annealing and running 100 cycles of charging and discharging. This structure matches with an orthorhombic perovskite structure with Pnma space group ( $a_o \sim 5.45$  Å,  $b_o \sim 5.36$  Å and  $c_o \sim 7.67$  Å.) (b) after sintering at  $1250^\circ\text{C}$  followed by annealing. The structure matches to pseudotetragonal (orthorhombic) with very minute difference in a and b lattice parameters  $\sim a_p \times a_p \times 2 c_p$  ( $3.82$  Å  $\times$   $3.81$  Å  $\times$   $7.68$  Å) that may be considered as to tetragonal lattice with P4/mmm symmetry (c) after sintering at  $1250^\circ\text{C}$  followed by quenching. The structure matches to an orthorhombic structure ( $\sqrt{2} a_p \times \sqrt{2} a_p \times 2 c_p$ ,  $5.43$  Å  $\times$   $5.41$  Å  $\times$   $7.66$  Å) with Pnma space group.
- Figure 5.3 Electron micrographs of  $\text{Li}_{0.48}\text{Nd}_{0.5}\text{TiO}_3$  sample after sintering at  $1250^\circ\text{C}$  for 24 hours 119  
followed by annealing, bright field image and corresponding electron diffraction pattern along (a, d)  $[11\bar{1}]$ , (b, e)  $[001]$  and (c, f)  $[0\bar{2}1]$  zone axis.
- Figure 5.4 Electron diffraction pattern of  $\text{Li}_{0.48}\text{Nd}_{0.5}\text{TiO}_3$  sample after sintering at  $1250^\circ\text{C}$  for 24 120  
hours followed by quenching and annealing considering (a) orthorhombic  $\alpha'$  phase with  $a = 5.41$  Å,  $c = 7.68$  Å along  $[111]$  zone axis (b) cubic A-phase with  $a = 3.83$  Å along  $[011]$  axis.
- Figure 5.5 Figure 5.5. Atomic structure of  $\text{Li}_{0.48}\text{Nd}_{0.5}\text{TiO}_3$  sample after sintering at  $1250^\circ\text{C}$  for 24 121  
hours followed by annealing with (a) 100 as projection vector and 010 upward vector (b) 100 as projection vector and 001 as upward vector (c) the composite of (a) and (b). (d) electron diffraction pattern along  $[100]$  zone axis showing two separate ordered supercell marked in red and black (e) atomic arrangement in the crystal structure of single domain of  $\text{Li}_{0.48}\text{Nd}_{0.5}\text{TiO}_3$  with 010 as projection vector and 001 as upward vector (f) 100 as the projection vector 010 as upward vector exhibiting ordering in (001) and (012) planes.
- Figure 5.6 3D elemental map of Li, Nd, Ti, and O in  $\text{Li}_{0.48}\text{Nd}_{0.5}\text{TiO}_3$  represented by their 123  
respective iso-concentration surfaces with two different orientations (a-b) Nd iso-concentration surface map of at 30 at% shows a complementary modulation of Ti and Nd concentration with a half wavelength of  $\sim 7\text{nm}-12\text{nm}$  (c-d) Li iso-concentration surface map at 28 at% in combination with Nd atomic position exhibits an alternative distribution of Li concentration.
- Figure 5.7 Electrochemical graphs of a  $\text{Li}_{0.45}\text{Nd}_{0.5}\text{TiO}_3$  sample after sintering at  $1250^\circ\text{C}$  for 24 125  
hours followed by quenching and annealing (a) voltammogram with a scan rate  $0.2 \text{ mVs}^{-1}$  (b) voltage Vs Specific capacity (charge-discharge profile) at C/2 (c) Specific capacity Vs Cycle number Vs coulombic efficiency. (d, e, f) similar electrochemical graphs of  $\text{Li}_{0.45}\text{Nd}_{0.5}\text{TiO}_3$  sample after sintering at  $1250^\circ\text{C}$  for 24 hours followed by

## LIST OF FIGURES

---

	quenching. (g, h, i) similar electrochemical graphs of $\text{Li}_{0.35}\text{Nd}_{0.5}\text{TiO}_3$ sample after sintering at 1250 °C for 24 hours followed by annealing.	
Figure 6.1	XRD patterns for $\text{ZnGaMnO}_4$ (a) heat treatment establishment (b) stoichiometry establishment.	136
Figure 6.2	XRD patterns of $\text{ZnGaMnO}_4$ , $\text{Co}_{0.6}\text{Fe}_{0.8}\text{Mn}_{1.6}\text{O}_{4+\delta}$ , $\text{Co}_{0.6}\text{Fe}_{0.8}\text{GaMn}_{1.6}^{+4}\text{ZnO}_{8+\delta}$ , and $\text{Co}_{0.6}\text{Fe}_{0.8}\text{Ga}(\text{Mn}_{1.6}^{+3}+\text{Mn}_1^{+4})\text{ZnO}_{8+\delta}$ , where $\delta \ll 1$ (a) sintered at 1250 °C for 24 hours followed by quenching in ice water (b) sintered at 1250 °C for 24 hours followed by quenching in ice water and aged at 375 °C for 150 hours.	138
Figure 6.3	Bright field image and corresponding electron diffraction pattern of $\text{Co}_{0.6}\text{Fe}_{0.8}\text{Ga}(\text{Mn}_{1.6}^{+3}+\text{Mn}_1^{+4})\text{ZnO}_{8+\delta}$ sample sintered at 1250 °C for 24 hours and quenched into ice water followed by ageing at 375 °C for (a) 25 hour (b) 75 hours (c) 150 hours. Here different type of Zone axis (two fold and four fold) were taken to visualized different appearance of the microstructure (g) dark field image corresponding to (c) considering 022 spot.	139
Figure 6.4	Bright field image of $\text{Co}_{0.6}\text{Fe}_{0.8}\text{GaMn}_{2.6}\text{ZnO}_{8+\delta}$ after sintering at 1250 °C and aging at 375 °C for 150 hour (a) herringbone-like appearance of microstructure, here strip-like domains are sharing thick interface (b) CB-like appearance of same microstructure and (d) corresponding electron diffraction pattern along $[\bar{1}\bar{1}\bar{1}]$ zone axis showing twinning in (202) planes.(c) magnified view of one domain in (b). (e) schematic representation of all the twinning elements involved.	141
Figure 6.5	(a-d) Bright field diffraction contrast images along $[\bar{2}\bar{3}\bar{3}]$ zone axis illustrating strip-like appearance CB-like microstructure at various tilt conditions at (a) $\alpha = 20.1^\circ$ it resembles a layered interface, (b) $\alpha = 4.8^\circ$ it shows alternative strips with four different contrasts (marked by numbers) representing an intriguing microstructure with domains of different mutual orientation and width. (c) an edge-on view of (b). (e) corresponding electron diffraction pattern for (b). (f) electron diffraction pattern for edge-on view shown in (c).	143
Figure 6.6	The X-ray Photoelectron spectroscopy (XPS) graphs of $\text{CoFeGaMnZnO}_{8+\delta}$ are showing oxidation sates of constituent elements (a) Co (b) Fe (c) Mn (d) Ga (e) O (f) Zn.	145
Figure 7.1	Schematic illustrates design procedure for 2D alternative growth of different nanorods using CB-like microstructure as a template. (a) the first step of the process shows selective growth of one type of nanorods (white) (b) the second step shows secondary deposition for another kind of nanorods (yellow).	154

## LIST OF FIGURES

---



### Abbreviations

<b>CB</b>	:	<b>C</b> hess <b>b</b> oard
<b>SD</b>	:	<b>S</b> pinodal <b>D</b> ecomposition
<b>TEM</b>	:	<b>T</b> ransmission <b>E</b> lectron <b>M</b> icroscope
<b>APT</b>	:	<b>A</b> tom <b>P</b> robe <b>T</b> omography
<b>LEAP</b>	:	<b>L</b> ocal <b>E</b> lectrode <b>A</b> tom <b>P</b> robe
<b>TOF</b>	:	<b>T</b> ime <b>o</b> f <b>F</b> light
<b>STEM</b>	:	<b>S</b> canning <b>T</b> ransmission <b>E</b> lectron <b>M</b> icroscope
<b>HAADF</b>	:	<b>H</b> igh <b>A</b> ngle <b>A</b> nnular <b>D</b> ark <b>F</b> ield
<b>SADP</b>	:	<b>S</b> electe <b>d</b> <b>A</b> rea <b>D</b> iffraction <b>P</b> attern
<b>BF</b>	:	<b>B</b> right <b>F</b> ield
<b>DF</b>	:	<b>D</b> ark <b>F</b> ield
<b>DCI</b>	:	<b>D</b> iffraction <b>C</b> ontrast <b>I</b> maging
<b>FFT</b>	:	<b>F</b> ast <b>F</b> ourier <b>T</b> ransform
<b>XEDS</b>	:	<b>X</b> -ray <b>E</b> nergy <b>D</b> ispersive <b>S</b> pectroscopy
<b>NBD</b>	:	<b>N</b> ano <b>B</b> eam <b>D</b> iffraction
<b>HRTEM</b>	:	<b>H</b> igh <b>R</b> esolution <b>T</b> ransmission <b>E</b> lectron <b>M</b> icroscopy
<b>CTF</b>	:	<b>C</b> ontrast <b>T</b> ransfer <b>F</b> unction
<b>XRD</b>	:	<b>X</b> -ray <b>D</b> iffraction
<b>SA</b>	:	<b>S</b> elf- <b>A</b> ssembly
<b>SSA</b>	:	<b>S</b> tatic <b>S</b> elf- <b>A</b> ssembly
<b>DySA</b>	:	<b>D</b> ynamic <b>S</b> elf- <b>A</b> ssembly
<b>MM</b>	:	<b>M</b> etamaterial
<b>ASSLBs</b>	:	<b>A</b> ll <b>S</b> olid <b>S</b> tate <b>L</b> ithium-ion <b>B</b> attery
<b>SSEs</b>	:	<b>S</b> olid <b>S</b> tate <b>E</b> lectrolytes
<b>SLRO</b>	:	<b>L</b> ong <b>R</b> ange <b>O</b> rd <b>e</b> r <b>P</b> arameter
<b>J-T</b>	:	<b>J</b> ahn- <b>T</b> eller <b>D</b> istortion
<b>CO</b>	:	<b>C</b> harge <b>O</b> rd <b>e</b> ring
<b>MCO</b>	:	<b>M</b> ulticomponent <b>O</b> xide

**Symbols**

$\theta$	:	Bragg angle
$\lambda$	:	Wavelength
$\beta$	:	Peak broadening
$t$	:	Crystallite size
$\Delta H$	:	Enthalpy of formation
$\varepsilon$	:	Misfit strain
$\Delta G$	:	Free energy
$d$	:	Interplanar spacing
$\gamma$	:	Surface energy
$a$	:	Lattice parameter
$^{\circ}$	:	Degree
$\epsilon$	:	Strain
$c$	:	Elastic constant
$k$	:	Shape factor
$\delta$	:	Small fraction
$\Delta$	:	Large fraction

## Preface

An exponentially growing demand for materials, advanced in terms of directional-multi-functionality of physical properties, has been witnessed in modern days nano-electronics. Here the term ‘directional’ is intended to mean the anisotropy of physical properties along different directions. This implies that the single component made of such materials will exhibit physical properties in various possible combinations, e.g., multi-magnetism, multiferroicity, optoelectronic, thermoelectricity, piezoelectricity etc. along different crystallographic directions. In addition, some applications require the miniaturization of electronic devices in order to produce compact equipment. However, one way to meet this demand is to fabricate materials with exotic microstructures consisting of well-organized periodically distributed phases in complex geometries, i.e. chessboard (CB) nanodomains. Such well-organized microstructures are achievable not only via some modern and hard-to-scale up techniques such as e-beam lithography, templated chemical vapor deposition and pulsed laser deposition etc. but also with various classical phase transformation routes, such as spinodal decomposition, pearlitic transformation, order-disorder transformation ( $A1$  to  $L1_0+L1_2$ ), martensitic transformation, intergrowth, and 3D self-assembled checkerboard-like (CB) microstructural evolution etc. However, most of the above-mentioned techniques produce lamellae, well-organized precipitates and nanowires, which have been well understood and reported. Among all the techniques mentioned above, CB like microstructural evolution is found to be the most suitable for the given applications. It has unique potency to produce 3D well-organized interlacing of two chemically separable and structurally distinct cuboidal nanodomains, possessing functionality of the desired properties. Top of all, the CB-like microstructural domains are reportedly pretty homogeneous in terms of size, shape, and compositional distribution. The physical properties of a multiphase material depend not only on the atomic structure of each constituent phase but also on their shape, size, and morphological distribution. Herein, we have studied the mechanism of CB-like microstructural evolution in spinel and perovskite systems.  $\text{CoFeMnO}$ ,  $\text{ZnGaMnO}$  and  $\text{CoFeGaMnZnO}$  multicomponent (MCO) spinel systems may evolve as CB microstructures consisting of well-organized nanodomains with differential functionality. In CB microstructure, well-organized alternative distribution of ferromagnetic and paramagnetic nanodomains builds up the decoupling effect of the magnetic

## PREFACE

---

moments that provides the required anisotropy to upgrade ultrahigh density recording medium ( $> 1 \text{ Tb/inch}^2$ ) to a state-of-the-art stage. The square faceted domains improve the archivability of the memory device. On the other hand, CB-like microstructural evolution in  $\text{LiNdTiO}_3$  perovskite system has been explored to comprehend its potential in all-solid-state lithium-ion battery (ASSLBs) applications. In this thesis, we have explored the evolution mechanism of CB-like microstructure in CoFeMn-based spinel,  $\text{LiNdTiO}_3$  perovskite and its effects on the physical properties.

All samples were prepared by solid-state synthesis route due to its potency to produce the pure and certain end products, ease of material handling and better reproducibility. High purity precursors ( $> 99.9\%$ ) were mixed in appropriate stoichiometries and were put through specific heat treatments. For CoFeMnO, ZnGaMnO and CoFeGaMnZnO based CB systems, precursor powders of  $\text{Fe}_2\text{O}_3$ ,  $\text{Co}_3\text{O}_4$ ,  $\text{Mn}_2\text{O}_3$ , ZnO, and  $\text{Ga}_2\text{O}_3$  were mixed and were pelletized in corresponding  $\text{Co}_{0.6}\text{Fe}_x\text{Mn}_{2-x}\text{O}_4$ ,  $\text{ZnGaMnO}_4$  and  $\text{Co}_{0.6}\text{Fe}_{0.8}\text{GaMn}_{2.6}\text{ZnO}_{8+x}$  stoichiometries. All the green pellets were sintered in air at  $1250 \text{ }^\circ\text{C}$  for 24 hours, followed by quenching in ice water. The sintering process was repeated twice with an intermediate grinding of the first time sintered and quench pellets to ensure a homogeneous composition throughout the sintered pellet. In order to obtain sufficient diffusive rearrangement of ions, ageing treatment was given in air atmosphere at  $375 \text{ }^\circ\text{C}$ . Similarly, to develop CB-like microstructure in  $\text{LiNdTiO}_3$  perovskite system, ultra-high pure precursor powders of  $\text{Nd}_2\text{O}_3$ ,  $\text{TiO}_2$ , and  $\text{Li}_2\text{CO}_3$ , were mixed and were pelletized in four stoichiometric ratios ( $0.16 > x > 0.05$ ),  $\text{Li}_{0.15}\text{Nd}_{0.5}\text{TiO}_3$ ,  $\text{Li}_{0.24}\text{Nd}_{0.5}\text{TiO}_3$ ,  $\text{Li}_{0.36}\text{Nd}_{0.5}\text{TiO}_3$  and  $\text{Li}_{0.48}\text{Nd}_{0.5}\text{TiO}_3$ . The pellets were sintered at  $1250 \text{ }^\circ\text{C}$  for 24 hours and were cooled through two different routes namely: prolonged annealing and ice water quenching, in order to develop chessboard-like microstructure and disordered bulk microstructure, respectively. The electrochemical performance of the samples was evaluated against the Li reference electrode. The electrochemical performance of each obtained product was evaluated with a 2032 coin-type cell using a non-aqueous electrolyte (1M  $\text{LiPF}_6/\text{EC}:\text{DMC}=1:1$  in volume) and a polypropylene separator (Celgard 3501) against lithium metal. The cells were assembled in a glovebox filled with high purity argon. Electrochemical cycling was performed within the voltage range of  $0.01\text{--}3\text{V}$  (vs.  $\text{Li}/\text{Li}^+$ ) at the scan rate of  $0.2\text{mVs}^{-1}$  at  $25 \text{ }^\circ\text{C}$ .

It was speculated that the chessboard like nanostructure evolves through a series of phase transformations. In order to closely investigate these intermediate phase transformation events, total ageing time, from quenching to equilibrium, has been divided into four successive slots,

## PREFACE

---

i.e., 0 hour, 5 minutes, 25 hours, 100 hours and 250 hours. In order to study these intermediate stages, samples at different stages of growth have been extensively investigated with XRD in combination with correlative microscopy of TEM and APT. In correlative microscopy, precise 2D information gathered by TEM investigations in various operating modes such as DCI, HAADF-STEM and HRTEM are complemented with the 3D information obtained by APT. The high-quality data has been processed with various software, i.e., Multislice image simulation, Rietveld refinement, and Vesta. Multislice image simulation has been performed with JEMS software to characterize complex structures, mainly interfacial arrangement of the nanodomains.

The XRD patterns corresponding to sintered and quenched conditions suggest that during the sintering treatment, the system was solutionized, which on quenching turned into unstable cubic  $\text{Co}_{0.6}\text{Fe}_{0.8}\text{Mn}_{1.6}\text{O}_4$  spinel phase. The peak positions of this unstable phase closely match  $\text{CoFe}_2\text{O}_4$  cubic spinel phase (JCPDS card number 00221086), which follows  $\text{Fd}\bar{3}\text{m}$  space group. This cubic matrix turns into tetragonal through a fast cubic to tetragonal phase transformation. The XRD peaks corresponding to this tetragonal matrix match with  $\text{CoMn}_2\text{O}_4$  tetragonal spinel phase (JCPDS card number 0011126), which follows  $\text{I4}_1/\text{amd}$  space group. This cubic to tetragonal polymorphic phase transformation involves an exchange of interstitial position between  $\text{Mn}^{+3}$  and  $\text{Fe}^{+3}$  ions, which stabilizes the crystal field energy in the spinel structure. Once the  $\text{Mn}^{+3}$  ion occupies the B octahedral void it becomes J-T active ion. The diffusion of J-T (Jahn-Teller distortion) active  $\text{Mn}^{+3}$  ion introduces the anisotropy in the primary unstable cubic phase and turns it into a metastable tetragonal phase. That leads to a phase separation of the phases consisting of J-T active and inactive ions. Ideally,  $\text{CoFe}_2\text{O}_4$  spinel structure possesses  $\text{Fd}\bar{3}\text{m}$  space group, but after phase separation induced by J-T active  $\text{Mn}^{+3}$  ion, another  $\text{CoMn}_2\text{O}_4$  tetragonal phase with  $\text{I4}_1/\text{amd}$  space group comes into co-existence. The bright-field image along [100] zone shows chessboard like microstructure consisting of well-organized bright and dark nanodomains. This intriguing CB like contrast is the consequence of the mutual orientation of the neighboring cuboidal domains. The rotationally aligned electron diffraction pattern shows four split spots along 004 and 040 planes. These four spots represent two cubic and two tetragonal phase orientation variants, sharing twinned interfaces along (022) and (02 $\bar{2}$ ). Tetragonal phase variants are in the twin relationship along (022) and (02 $\bar{2}$ ); one tetragonal variant is rotated 180° around axis perpendicular to (022) or (02 $\bar{2}$ ) planes of another tetragonal variant. The domains that have gone out of Bragg's diffraction condition appear bright, and those satisfying the condition

appear dark. The high-angle annular dark-field scanning transmission electron microscopy (HAADF-STEM) was performed on the post-annealed, phase-separated sample evidencing that these bright and dark nanodomains represent Fe-rich and Mn-rich phases. The orientation relationship between the cuboidal domains of cubic and tetragonal phases ought to be  $\sim 5.2^\circ$  at the interface to minimize the strain induced by a misfit in lattice parameters. In the case of chessboard microstructure,  $\gamma_{\text{chemical}} = 6a^2\gamma_c$ ,  $\gamma_{\text{structure}} = a^3.c\varepsilon.\gamma$ , where  $c$  is elastic constant and  $\varepsilon$  is misfit strain and can be calculated by  $\varepsilon = \frac{(a_c - a_t)}{(c_t - a_c)}$ , here  $a_c \sim 8.3 \text{ \AA}$ ,  $a_t \sim 8.1 \text{ \AA}$  and  $c_t \sim 8.8 \text{ \AA}$ . In some unique situations, the series of nanodomains lying in the identical Bragg's diffraction condition resembles a continuous rod. In this study, we have observed the formation of subdomains for the first time. Critical analysis of APT results has provided evidence of subdomains up to three-levels. At the First level CB microstructure shows domains of the order of 70nm x 70nm, while on the later levels, it shows subdomains of 10 nm x10 nm and 2 nm x 2 nm in the same sample. This observation suggests that CB-like microstructural evolution involves a recurring phase separation, where a coherent strain derives the 3D self-assembling of orientation variants. The facets of the domain generally grow normal to elastically soft directions of the crystal structure. In the same experiment, we have observed that spinodal decomposition leads to the formation of subdomains of higher compositional difference than their parental domains. Simultaneously, this compositional phase separation coalescence of parental domains along 040 or 004 directions turns cuboidal nanodomains into rods with facets along 022 and  $(02\bar{2})$  planes. In the same line, ZnGaMnO and CoFeGaMnZnO were also investigated in order to understand CB evolution in them. Synthesis of a spinel based CoFeGaMnZnO MCO and formation of CB-like microstructure in any MCO is an entirely new observation. In the corresponding investigations we have found that the evolution mechanism in ZnGaMnO<sub>4</sub> and Co<sub>0.6</sub>Fe<sub>0.8</sub>GaMn<sub>2.6</sub>ZnO<sub>8+δ</sub> ( $\delta \ll 1$ ) based spinel system is similar to Co<sub>0.6</sub>Fe<sub>0.8</sub>Mn<sub>1.6</sub>O<sub>4+x</sub> ( $x \ll 1$ ). However, the evolution kinetics is relatively sluggish in the case of MCO. In the ZnGaMnO<sub>4</sub> system, the system was separated into two coexisting phases having composition near to  $\sim \text{ZnGa}_2\text{O}_4$  and  $\sim \text{ZnMn}_2\text{O}_4$  phases. On the other side, Co<sub>0.6</sub>Fe<sub>0.8</sub>GaMn<sub>1.6</sub><sup>+3</sup>Mn<sub>1</sub><sup>+4</sup>ZnO<sub>8+δ</sub> has formed CB nanodomains of the order of 7 nm x 7 nm in four different contrast. However, the HAADF-STEM-EDS maps could not differentiate the composition in the neighboring domains. These results refer to two different possibilities. First, the chemistry of cubic and tetragonal domains is of mixed nature. Second, there is only a subtle difference in the relative composition of four neighboring nanodomains that EDS detector is unable to distinguish.

## PREFACE

---

A similar study shows that in sintered-quenched and annealed  $\text{Li}_{0.48}\text{Nd}_{0.5}\text{TiO}_3$ , Nd-ions, Li-ions, and vacancies are distributed in perovskite A-site and are ordered within alternate (001) planes. Ordering along 001 direction doubles the c-parameter of the primitive perovskite structure and turns it into a pseudo-tetragonal structure with Pmmm space group. The combined effect of the vacancy and aliovalent substitution slightly distorts the structure to pseudo-tetragonal (orthorhombic) with a minute difference in a and b lattice parameters  $a_p \times 2 c_p$  (3.82 Å x 3.81 Å x 7.68 Å) that still can be considered as a tetragonal lattice with P4/mmm symmetry. In contrast, the crystal structure of a sintered and quenched  $\text{Li}_{0.48}\text{Nd}_{0.5}\text{TiO}_3$  sample shows an orthorhombic crystal symmetry (Pmmm) with  $a_p \times a_p \times c_p$  (5.45 Å x 5.36 Å x 7.67 Å). Such a structural change is ascribed to the disordering of Nd-ions, Li-ions, and vacancies at A-site. In general,  $\text{LiNdTiO}_3$  system shows four polymorphs A (primitive cubic),  $\alpha'$  ( $\sqrt{2} a, \sqrt{2} a + \delta, 2a - \delta$  tetragonal, where  $\delta$  is small distortion), C (orthorhombic distortion of  $\alpha'$ ), and  $\beta$  (tetragonal with  $a, a, 2a + \Delta$ ) where  $\Delta$  is a large distortion. XRD analysis shows that  $\text{LiNdTiO}_3$  sample, sintered at 1250 °C followed by quenching, acquires an orthorhombic  $\alpha'$  symmetry. On the other hand, same sample after sintering and annealing attains a tetragonal  $\beta$  symmetry through a polymorphic transformation. Rietveld refinement of sintered-annealed  $\text{Li}_{0.48}\text{Nd}_{0.5}\text{TiO}_3$  confirms the formation of  $\beta$  phase in which ordering of aliovalent cations and vacancy distribution at A-site accounts for the variation in the Ti-O bond lengths. The difference in six Ti-O bond lengths introduces significant distortion in the unit cell, providing an off-center shift to  $\text{Ti}^{+4}$  cations that result in octahedral  $\text{TiO}_6$  tilting. Bright-field image along the [001] zone axis shows two alternative bright and dark strip regions like nanodomains sharing interfaces along [100] and [010] directions. The corresponding electron diffraction pattern shows the superimposition of two mutually perpendicular diffraction patterns representing two domains having 001 direction perpendicular to each other. The interpenetration of these two striped nanodomains gives birth to CB-like microstructure. In addition, APT investigation of the same sample suggests the role of compositional phase separation in CB evolution. The iso-concentration surface maps suggest a difference in Ti, Li and Nd concentrations at both sides of isosurfaces of the corresponding element. From this correlative evidence, combined with these phase transformation complexities, spinodal decomposition gives birth to the nano chessboard-like microstructure consisting of 3D well-organized alternative domains.

Parallel to the abovementioned microstructural investigation, we have also studied how the CB-like microstructural evolution affects the electrochemical properties of the  $\text{LiNdTiO}_3$  samples. The coulombic efficiencies and specific capacities of both the samples are almost

## PREFACE

---

equal in the beginning of the charging-discharging cycles, i.e. coulombic efficiency  $\sim 99\%$  and specific capacity  $\sim 120 \text{ mAhg}^{-1}$ . The coulombic efficiency and specific capacity of the sintered-annealed  $\text{Li}_{0.48}\text{Nd}_{0.5}\text{TiO}_3$  sample remains constant at  $\sim 99\%$  and  $\sim 120 \text{ mAhg}^{-1}$  even after 100 cycles. Whereas, for sintered-quenched  $\text{Li}_{0.48}\text{Nd}_{0.5}\text{TiO}_3$  (disordered) sample-specific capacity reduces from  $120 \text{ mAhg}^{-1}$  to  $100 \text{ mAhg}^{-1}$  ( $\sim 16\%$ ) with no change in coulombic efficiency. Compared to sintered-annealed  $\text{Li}_{0.48}\text{Nd}_{0.5}\text{TiO}_3$  samples, the specific capacity of the  $\text{Li}_{0.36}\text{Nd}_{0.5}\text{TiO}_3$  sample is relatively less ( $110 \text{ mAhg}^{-1}$ ) in the beginning of the charging and discharging cycle with  $\sim 99\%$  coulombic efficiency. In sintered-annealed  $\text{Li}_{0.36}\text{Nd}_{0.5}\text{TiO}_3$  sample, a drastic decrease in specific capacity was observed ( $27\%$ ) after 100 cycles.

The abovementioned investigations suggest that the mechanism of evolution for CB like microstructure is system dependent and for spinel systems, it is quite different from perovskite systems. However, the formation of the symmetry-breaking phase is common in both systems.